Heritage Science

RESEARCH

Open Access

Biofouling and biomineralization of tubular concretions attached to Longquan celadon from Shengbeiyu shipwreck, China (14th Century CE): a multi-analytical case study

Xinyi Liu[1], Yu Li[2], Jianrui Zha[1], Xiangna Han[1*] and Hao Wang[3*]

Abstract

A comprehensive multi-analytical investigation was conducted on a piece of Longquan celadon excavated from the Shengbeiyu shipwreck site in the East China Sea. This study focused on a representative type of tubular bio-concretions attached to the submerged celadon, believed to have been formed through the construction activities of a marine tubeworm belonging to the benthic phylum of *Polychaeta Annelids*. The research examined the micro-structure, composition and adhesion form of these tubular bio-concretions, aiming to elucidate their developmental and attachment patterns from a biomineralization and biofouling perspective. The tubular bio-concretions were found to have a bimineralic composition, with notably higher content of aragonite than calcite, and display diverse yet highly ordered microstructures. The presence of organic matter within the bio-concretions indicates an organic matrix-controlled crystallization model, commonly observed in the construction of benthic calcareous tubes. Micro-scopic analyses revealed the primary degradation microstructures and corresponding phases of the glaze to which calcareous tubes attached. These findings closely resembled the corrosion characteristics observed in submerged ceramic glaze without bio-concretion attachments, as documented in earlier studies. OM and SEM observations also indicated that the calcareous tubes intricately intermeshed with the cracked glaze layer of the celadon. Addi-tionally, Raman spectroscopic analysis detected the presence of proteins at the interface, likely residual adhesives secreted by fouling organisms to cement themselves to the settlement substrata, suggesting the occurrence of organic-mediated bio-adhesion mechanisms. These results shed new light on the formation process of bio-concre-tions and their interaction with attached underwater ceramics. A simplified formation mechanism of this biologically-induced degradation has been discussed.

Keywords Shengbeiyu shipwreck, Longquan celadon, Tubular concretion, Biomineralization, Biofouling

*Correspondence:
Xiangna Han
jayna422@ustb.edu.cn
Hao Wang
haow21@126.com
Full list of author information is available at the end of the article

Introduction

Situated at the intersection of the eastern and the southern routes of the ancient Maritime Silk Road, more than 10 underwater shipwreck sites have been discovered in the waters off the coast of Zhangzhou, Southeast China, to date [1]. Of particular interest is an underwater shipwreck from the Yuan Dynasty (1271–1368 CE), excavated near Shengbeiyu islet, owing to its extensive collection of Longquan celadon wares [2]. The underwater assemblage retrieved from the shipwreck site in 2023 contains a total of 16,383 pieces of Longquan celadon ceramics. This shipwreck reflects the peak of Longquan celadon's export during the late Yuan Dynasty. Buried beneath underwater sediments and stones at a depth of ~ 30 m [1–3], the shipwreck has undergone centuries of alteration processes induced by physical, chemical and biological factors within the surrounding marine environment, such as wave motion, salinity, sediments, and biological activities [4–6]. These multifaceted elements significantly contributes to the deterioration of the Longquan celadon onboard, particularly due to biological activities, including the colonization of microorganisms and macrobenthos [7, 8]. The inherent vulnerabilities of celadon, primarily associated with the glaze microstructure, such as the presence of internal bubbles, crystalline phases, phase-separation structures [9], micro-cracks on the outer surface, and other factors [10], render it susceptible to biofouling. Overall, biogenic calcareous concretions are commonly observed on the celadon excavated from the Shengbeiyu shipwreck site, primarily consisting of shells or skeletons constructed in situ by benthic organisms such as barnacles, bryozoans, serpulidae, and corals [8, 11]. Biofouling can alter the physicochemical properties of the local environment on the surface of submerged materials, thereby inducing localized corrosion, like pitting corrosion [12].

To ensure the preservation of underwater excavated celadon, a thorough understanding of the concretions is required for the development of a safe and efficient cleaning procedure to remove dense encrustations. Previous studies have focused on the categorization, mineral composition, and microscopic morphology of the concretions [5, 8, 13–17], as well as the effectiveness evaluation of treatment methods [16, 18] and cleaning materials [19, 20]. However, the existing literature concerning the biofouling and/or biomineralization aspects is notably lacking, although the phenomenon of biofouling attachment is highly prevalent on the surfaces of submerged cultural heritage, and their accumulated calcareous shells and skeletons result in significant destruction [7, 21]. Addressing this research gap is crucial to avoid inappropriate cleaning treatments.

In this study, we adopted methodologies from biomineralization and biofouling research [22–26] to investigate possible development and settlement patterns of the calcareous bio-concretions on celadon from Shengbeiyu Shipwreck, China (14th Century CE). Our research aims to provide a comprehensive understanding of calcareous bio-concretions, especially from the biomineralization and biofouling perspective. This knowledge will inform the future development of cleaning solutions, ensuring the safe and effective conservation of these invaluable underwater heritage objects.

Materials and methods

Archaeological background

The underwater wreckage unveiled near Shengbeiyu islet, off the coast of Zhangzhou in Southeast China 's Fujian Province (Fig. 1a), is situated in a submarine gully. The seabed in this area primarily consists of sandy sediment and rocks, with extensive reef rocks present in the northern part. Hydrographic surveys [27] indicate that the seawater in this region has a slightly alkaline pH of around 8.17 and a high dissolved oxygen concentration of ~ 8.44 mg/L. This suggests ample oxygenation, providing a well-aerated habitat for marine organisms such as benthic invertebrates. In addition, both the chemical oxygen demand and nutrient levels in the water are relatively low, implying limited organic pollution and nutrient enrichment. The average salinity of the seawater is 25‰ [28], and the annual average water temperature is 27.2 ℃.

Samples

An impaired ware of Longquan celadon, excavated from the Yuan Dynasty Shengbeiyu shipwreck site, has been selected as a representative case study for the present research and designated as SBY-1. The National Centre for Archaeology (the NCA) graciously provided this sample. Digital images capturing the internal and external surfaces of the sample are presented herein. The majority of the glaze layer is highly corroded, nearly opaque and extremely matte, rendering it an overall yellowish-brown appearance. The original greenish ceramic glaze has largely disappeared, and the surface of this sample is characterized by the attachment of a significant quantity of bio-concretions (Fig. 1b, c).

Based on preliminary investigations, the tubular bio-concretions have been identified as representative and consequently selected as the primary focus of this paper. A subset of samples related to the tubular bio-concretions found on the surface of ware SBY-1 was randomly selected and assigned numerical labels ranging from 01 to 12. Descriptions of each sampled section, along with the corresponding analytical methods employed, are documented in Table 1.

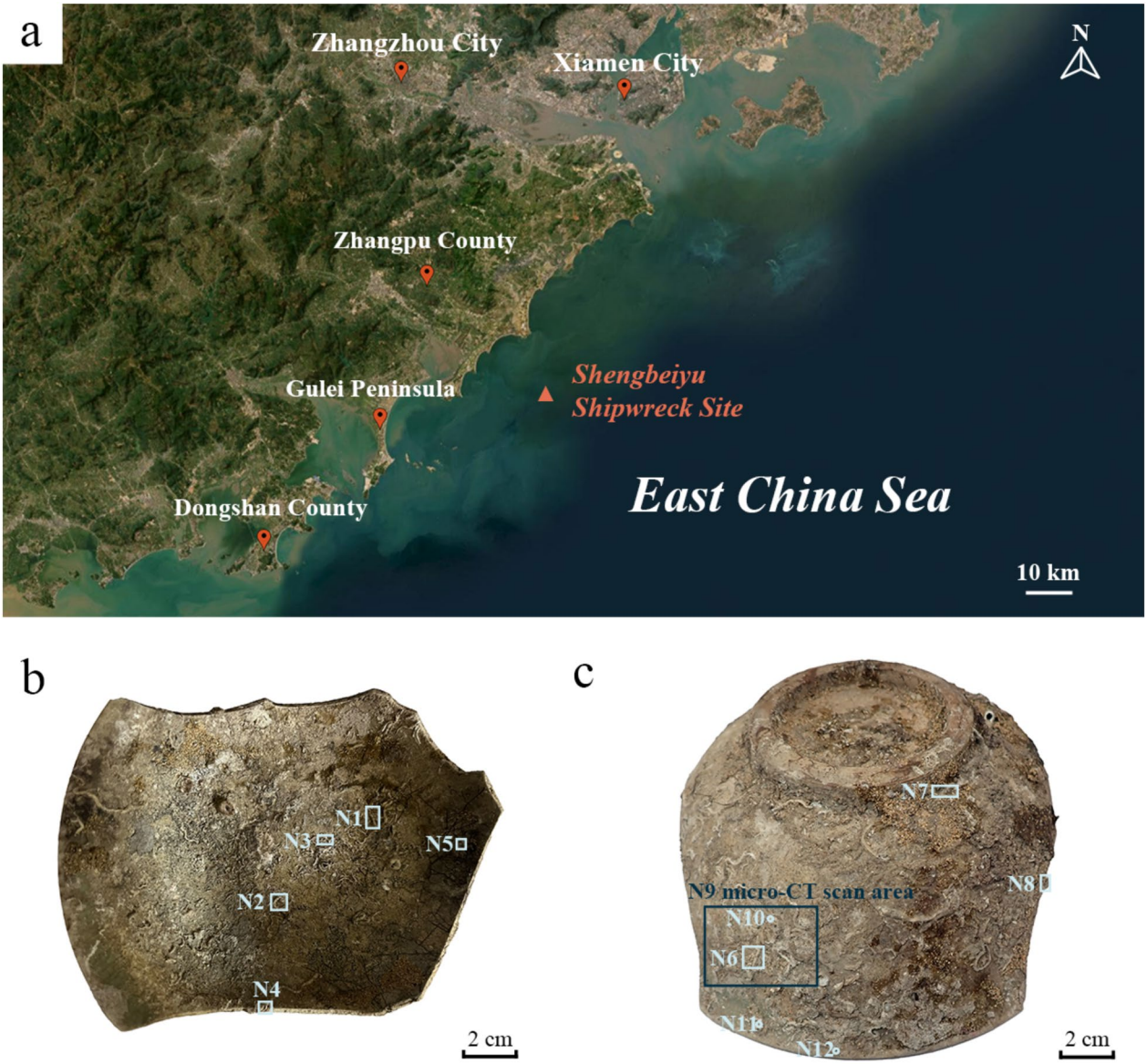

Fig. 1 Location of Shengbeiyu shipwreck site and the appearance of Longquan celadon ware sample SBY-1. **a** The geographical location of Shengbeiyu shipwreck site in Zhangpu county, Fujian province. The base map is a full-resolution images derived from the Level-1 and Atmosphere Archive & Distribution system (LAADS) data products, accessed via the GLOBAL Imagery Browse Services (GIBS) tile service and obtained through View Data Tool. (https://ladsweb.modaps.eosdis.nasa.gov/view-data/#@0.0,0.0,3.0z) [29] **b** the internal surface and **c** the external surface of sample SBY-1

Table 1 Descriptions of samples and corresponding analytical methods

Sample No.	Sample description	Characterization methods	Analysis purpose
N1–N8	Tubular bio-concretions	OM; XRD; FT-IR; Raman spectroscopy; TG-DTG	Concretion cognition
N9	Typical bio-colonization phenomena	OM; micro-CT	Concretion cognition & attachment pattern analysis
N10–N12	Tiny sherds with attached tubular bio-concretions	OM; SEM–EDS; Raman spectroscopy	Concretion cognition & attachment pattern analysis

Methods

A comprehensive characterization of the biogenic concretion was achieved through a multi-analytical study utilizing a range of techniques, including microscopic analysis, X-ray diffraction (XRD) analysis, thermal analysis, and spectroscopic analysis. The specific methodologies employed for complete characterization are detailed as follows:

Micro-Computed Tomography (micro-CT)

Micro-CT imaging data was acquired for sample N9 to enable non-destructive observations of sections from any point and direction. 3D segmentation and reconstruction were conducted using Drishti software. Sample N9 was divided into two parts, and CT scans were conducted twice using the Bruker SKYSCAN 1273 3D X-ray Microscopy. The first scan was performed without a filter, achieved a spatial resolution of 15.00 μm and a rotation step of 0.15 degrees. The second scan utilized an Al 1 mm + Cu 0.038 mm filter combination, resulting in a resolution of 13.31 μm while maintaining the same rotation step.

Microscopic observations

Optical microscopy (OM) and scanning electron microscopy (SEM) were employed for microscopic analyses. For species identification, recognition of bio-colonization phenomena, and macro-morphology investigation of the concretion-glaze binding interface, an initial investigation utilized a VHX-6000 3D ultra-depth-of-field optical microscope. Subsequently, SEM observations were conducted using a Tescan Vega3 and a Hitachi Regulus8100, both equipped with energy dispersive spectroscopy (EDS). These analyses facilitated a detailed examination of the tubular concretions, encompassing their microstructure, elemental compositions, and the organic matrix within the tube skeletal structure. Furthermore, SEM analyses were employed to investigate the typical degradation morphologies of the glaze as well as the interface morphologies between the tubular bio-concretions and the glaze. Prior to SEM analysis, all samples were subjected to a gold coating, and the microscopy session was carried out at a high voltage range of 10–15 kV.

X-ray diffraction analysis (XRD)

XRD were employed to investigate the overall mineral composition of the tubular concretions. Powdered samples were analysed on a Bruker D8 Advance X-ray diffractometer equipped with CuKα radiation. The testing parameters were carefully configured, with a 2θ scan ranging from 10° to 90°, a step size of 0.02°, and a scan speed of 0.03 s/step [26].

Thermogravimetric analysis (TGA)

TGA was applied to determine the content of the organic matrix within the tubular bio-concretions. The analysis was conducted using a NETZSCH STA 449 F3 instrument under a nitrogen atmosphere. Heating ranged from room temperature (RT) to 900 °C, with a heating rate of 10 °C /min. A minuscule amount of powdered sample N6 recovered from the previous XRD analysis was used as the specimen.

Spectroscopic analysis

Fourier transform infrared spectroscopy (FT-IR) and Raman spectroscopy were performed to study the mineral composition and provide preliminary identification of biomacromolecules such as protein or polysaccharides. FT-IR analyses were carried out using the Nicolet iS5 FTIR instrument, covering the 0–4000 cm^{-1} range with a nominal spectral resolution of 4 cm^{-1} and 32 scans. Raman spectra were obtained by HORIBA XploRA PLUS Raman Spectroscopy, ranging from 100 to 1700 cm^{-1}, with the window centered at 1618.08 cm^{-1} and the excitation of laser beam at 785 nm.

Results and discussion

Bio-colonization phenomena and preliminary species identification

Figure 2 provides an overview of the various principal calcareous bio-concretions present on the surface of sample SBY-1. These concretions display diverse morphologies, including tubular, porous, and dendritic calicular types. It is noteworthy that these three morphological types frequently coexist and interact on the surface of the celadons salvaged from the Shengbeiyu shipwreck site, as exemplified by the observed phenomena of symbiosis and epibiosis in panels a, b, and c. Through comparative analysis with previous studies on marine life typology [25, 30] and investigations into fouling organism community distributions, the calcareous skeletons or shells shown in Fig. 2d, e and f can tentatively be identified as belonging to the phyla of *Polychaeta Annelids*, *Bryozoa* and *Scleractinia*, respectively. In addition, it can be observed that the surface of this celadon ware sample is heavily encrusted with a considerable accumulation of sandy sediment and algae.

To gain a deeper understanding of the deposition of biological concretions and their intricate interrelation with the underlying glaze, we performed micro-Computed Tomography (micro-CT) on a typical area of sample SBY-1. The area scanned is demarcated by the blue box in Fig. 1b and the micro-CT data underwent

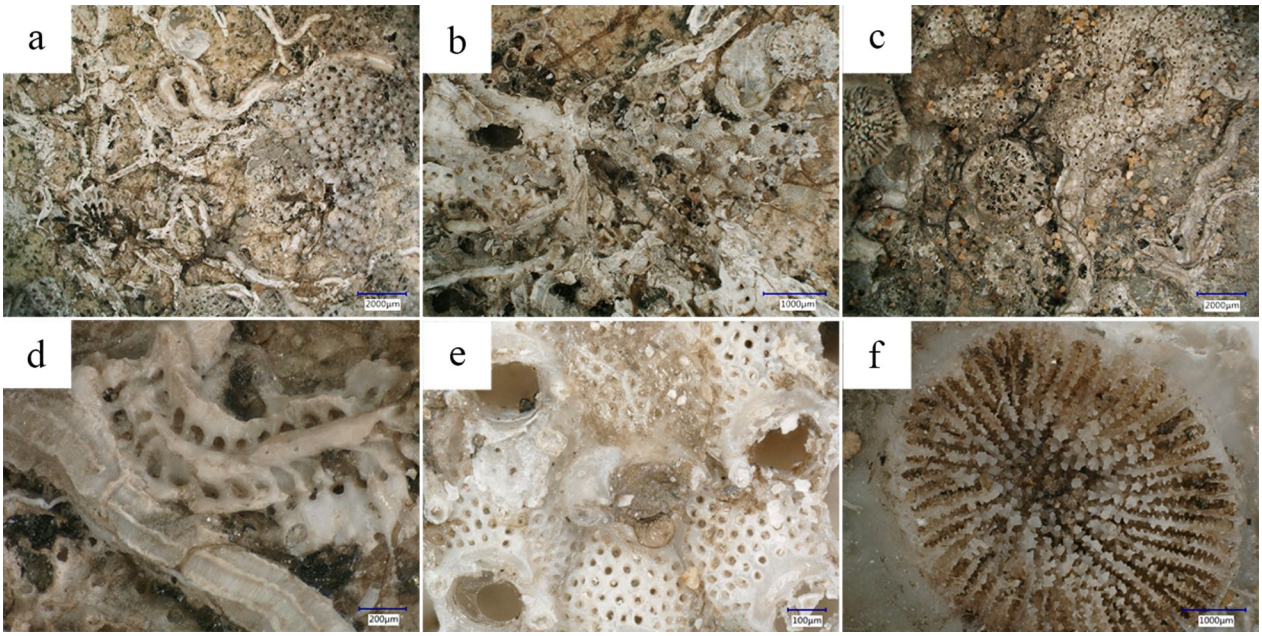

Fig. 2 Representative micrographs of biogenic preponderant groups on the surface of celadon sample SBY-1. **a**, **b** and **c** typical bio-colonization phenomena. **d** tubular concretion, **e** porous concretion, and **f** dendritic calicular concretion

processing using the Drishti software [31]. The 3D reconstruction and segmentation [32] results of micro-CT data are displayed in Fig. 3 below.

The Drishti software specializes in executing mathematical morphology operations such as morphological opening and closing, enabling effective differentiation between objects [33]. The micro-CT analyses enable clear three-dimensional visualization of the sedimentary structure, providing distribution characteristics and the attachment patterns of various bio-concretions. There are two noteworthy phenomena indicative of bio-colonization patterns.

Firstly, in addition to directly attaching to the surface of the celadon, both porous and tubular concretions may adhere to one another, potentially forming alternating layers. Secondly, the tubular concretions attached to glaze surface may induce uneven and rough textures, as illustrated in panel d. Drishti's 3D segmentation function allows for non-destructive examination of cross-sections in any region of interest, thereby preserving the original sedimentary layer information and facilitating erosion level assessments. As depicted in Fig. 3b and d, a closely intermeshed relationship between the tubes and the glaze is evident. It is further hypothesized that such biofouling may render the glaze susceptible to localized corrosion [34], such as stress corrosion cracking (SCC). Additional research has emphasized that matrix surface roughness plays a crucial role in benthos settlement and colonization [35]. Regions without bio-concretions, indeed, exhibit rough patches with a conspicuous layered structure (refer to panels a and c).

The Shengbeiyu sea area, located on the eastern edge of Gulei Peninsula, Zhangpu County (refer to Fig. 1a) harbors a diverse array of macrobenthic communities, including polychaeta, mollusks, and crustaceans [36]. Among the *polychaeta* species commonly discovered in the coastal waters of China's East Sea, *Hydroides elegans*, *Hydroides ezoensis* and *serpulid tubeworm* are particularly prevalent [37, 38]. The observed tubular bio-concretions exhibit a morphological resemblance to the calcareous outer tubes of these three types of *polychaeta* species. Therefore, it is suggested that the tubular bio-concretions were $CaCO_3$-walled tubes produced by fouling sedentary *polychaetes* belonging to the genus *Hydroides*, family *Serpulidae* [37].

Considering that a significant number of these tubular bio-foulers directly affect the surface of the sample SBY-1 and have the potential to cause further damage, our subsequent study focused on understanding their intrinsic composition, microstructure, and attachment patterns on the glaze layer. In addition, our research also attempted to discuss the possible role of these bio-concretions in the degradation process of the submerged celadon.

Microstructure and elemental composition of tubular bio-concretions

Tube ultrastructure and elemental composition were examined in cross-sectioned samples N10 and N11 using

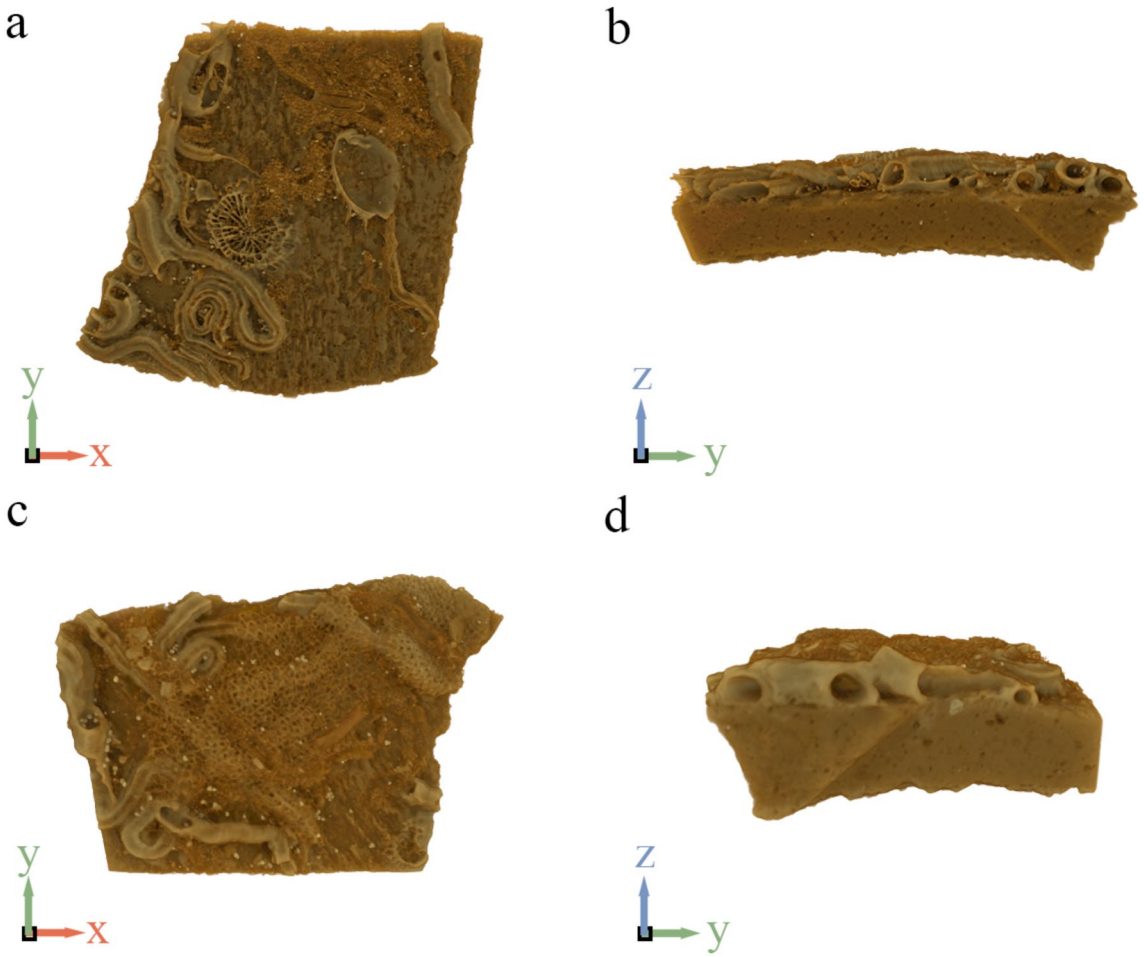

Fig. 3 3D visualization results of micro-CT data from sample N9 using the Drishti software. **a** and **c** the regions of interest selected on sample N9 using the Drishti software. **b** and **d** the lateral views of the regions of interest shown in **a** and **c**, respectively

OM and SEM, as depicted in Fig. 4. These two samples exhibited tubular bio-concretions attached to their surfaces. The specific mineral phases can be further determined by in-situ Raman spot analysis based on the compositional information obtained from EDS, which will be discussed in later chapter.

These bio-concretions exhibited a distinct layered structure, with certain textural layers displaying hierarchical lamellae structures spanning multiple length scales, ranging from the self-assembled nanoscale to the microscale and ultimately to the macroscale levels. Figure 5 below illustrates the specific arrangement: the third-order lamellae structure is composed of circular nanoparticles that preferentially align in specific orientations (Fig. 5b, d), assembling into fibrous second-order lamellae (see Fig. 5c) or rod-like morphologies with diameters ranging from ~ 400 to 600 nm (Fig. 5b); this secondary structure then organizes in a parallel direction, resulting in the formation of first-order lamellae. Such observations substantiate the characterization of tubular bio-concretions as hierarchical materials. The hierarchically ordered arrangements are believed to alleviate their own intrinsic weaknesses and brittleness, inhibit crack initiation and propagation, and facilitate high defect tolerance [39]. Consequently, such tubular bio-concretions might display enhanced mechanical properties, particularly in terms of strength and toughness, surpassing those of geological aragonite [22].

Furthermore, the inner macroscopic layer of the fracture surface exhibited higher porosity and irregularity in comparison to the outer side, indicating variations in microstructure and corresponding fracture modes. The presence of pores, stemming from pulled-out aragonite fibers, were observed in the inner layer, as indicated by the red arrows in Fig. 5b. The outer layer is composed of densely and orderly packed crystallites which can effectively protect the potentially fragile tube structures from dissolution and external attacks [40]. Vinn et al. [25, 41]

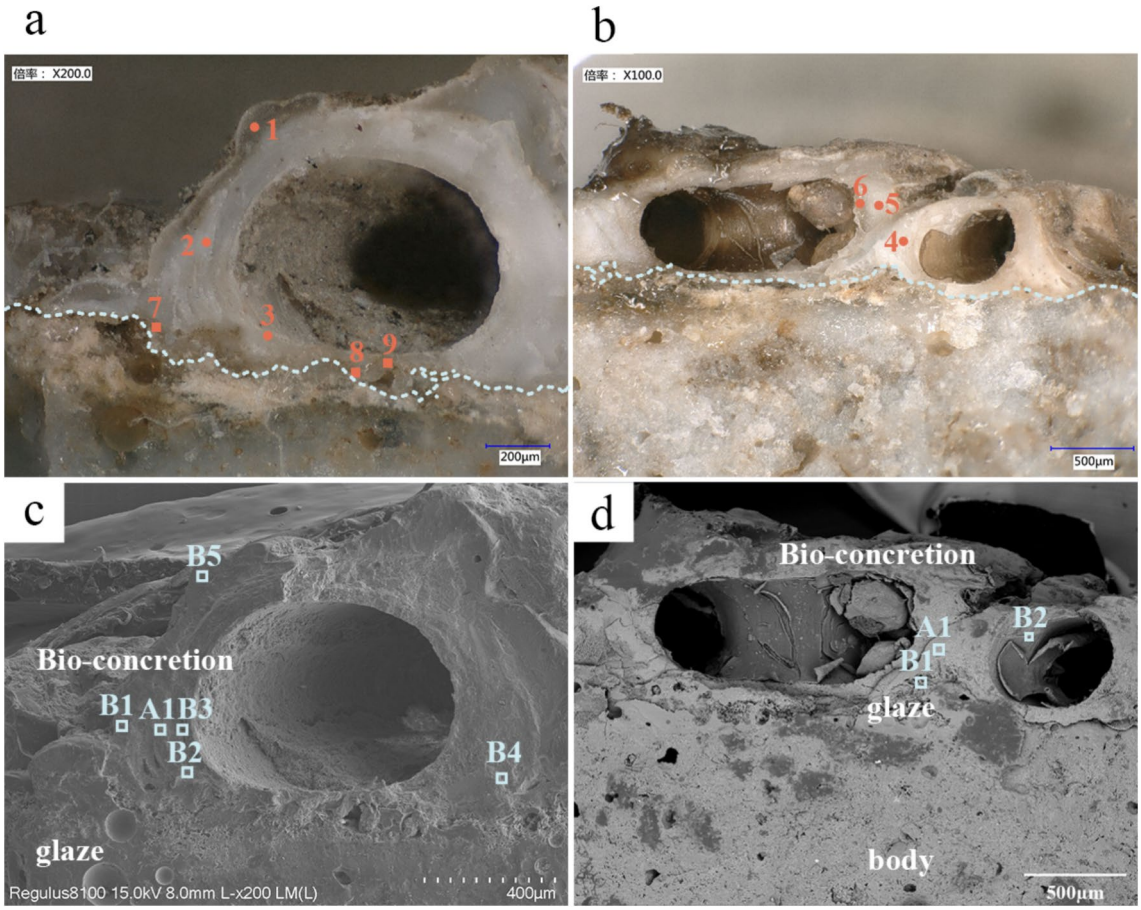

Fig. 4 Cross-sectioned surfaces of sample N10 and N11. **a** optical micrograph (200x) of sample N10, **b** optical micrograph (200x) of sample N11. **c** and **d** corresponding SEM images of **a** and **b**, respectively

have also reported the occurrence of two- or multi-layered tubes in *serpulids*, where the outer layer typically composed of dense mineral structures.

Marine bio-foulers possess remarkable capabilities in producing a diverse range of calcified materials, including granular, prismatic, lamellar, fibrous, foliated, and plywood-like microstructures, to construct their shells or skeletons [42]. Existing research has shown that *serpulids* exhibit 15 distinct types of mineral microstructures [43, 44], with lamella-fibrillar (LF), irregularly oriented prismatic (IOP), and spherulitic-prismatic fabrics (SPHP) constituting the major ultrastructural components [45]. Upon conducting a detailed examination of the tubular concretions using high-magnification SEM, two primary categories of microstructures were identified, namely granular and prismatic, as illustrated in Fig. 6a–f.

To be specific, Figs. 5b, d and 6a–c highlight the granular structure. These self-assembling nanoparticles are agglomerated and arranged in a two-dimensional direction to form microlayers. Figures 6a and b indicate that these nanoparticles can be semi-oriented or preferentially oriented, giving rise to a dense lamellar structure with closely-packed particles. Each of these particles measures ~ 40–60 nm in diameter and primarily consists of calcium carbonate without magnesium doping, as indicated in Table 2. Additionally, multiple electron microscopic images of different samples reveal the presence of a distinct type of lamellar structure composed of unoriented nanoparticles with an average size of 20 nm (Fig. 6c). EDS analyses demonstrate that the manganese (Mn) signal predominantly originates from this kind of lamellar structure. In the case of area P1 in Fig. 6c**,** Mn content was found to be as high as 11.34 wt%. The presence of this distinctive structural feature suggests the occurrence of ion exchange process within the bio-induced degradation system, whereby Mn is likely derived from the marine environment or the glaze layer. Mn is known to be abundant in the marine settings, while the XRF results reported in the archaeological investigation [46] indicated that there are also trace amounts of Mn within the glaze component of the analogous submerged celadon.

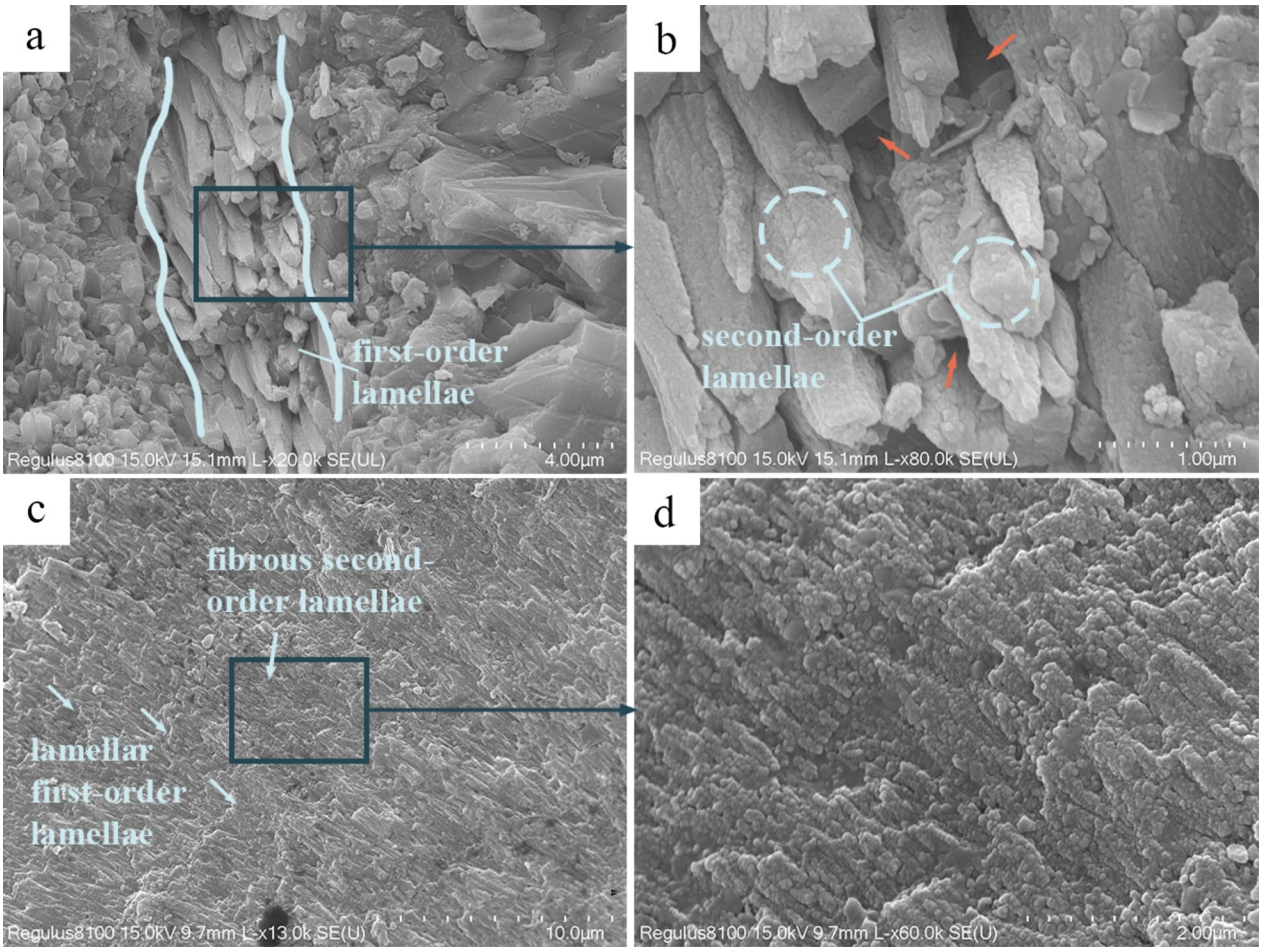

Fig. 5 Typical hierarchically ordered structures in tubular bio-concretions. **a** and **b** are the enlarged view of Fig. 4 **c** A1, while **c** and **d** are the enlarged view of Fig. 4 **d** A1

Figure 6d–e depict the prismatic structure, which can be classified into three types: irregularly oriented prismatic (IOP) structure (Fig. 6d); semi-ordered irregularly oriented prismatic (SOIOP) structure (Fig. 6e); and regular prismatic structure characterized by a uniform orientation of the crystal's elongation axis (Fig. 6h). These prismatic microstructures should be described as isotropic, semi-oriented, and oriented structures, respectively, consistent with the typical morphological characteristics observed within *serpulid* tubes [25]. The SEM images clearly show the highly ordered shape, uniform appearance, and flat surfaces of the prismatic structure. In Fig. 6, the diameter of each prismatic structure descends sequentially from left to right, while the elemental composition of that in d and e is highly similar, both consisting of aragonite without magnesium, as indicated in Table 2. The elemental composition of random regions across the cross-sectioned surfaces of tubular bio-concretions, obtained from EDS measurement, indicated the magnesium content is low or absent. It is widely accepted that calcite incorporates more Mg in the lattice structure compared to aragonite, and the Mg/Ca ratio is also a known elemental proxy of calcite [47]. Therefore, it can be preliminarily inferred that aragonite is the predominant mineral phase in this bio-concretion.

Moreover, the morphological and elemental composition data provide evidence for the existence of organic sheets within the mineral tube structure (Fig. 6g–i). Detailed analyses employing SEM–EDS reveal the presence of membrane-like substances with significantly high concentrations of carbon (C), nitrogen (N), phosphorous (P), and/ or sulfur (S). Specifically, in the case of Fig. 6gP1, the measured contents are as follows: 48.42 wt% C, 8.64 wt% N, 11.16 wt% S. Consistently, previous studies have indicated that carboxylated and sulfated polysaccharides are the principal components of the soluble organic matrix, which aligns with this high S content value [48, 49]. Similarly, both the C content of P1 in Fig. 6h and the N content of P1 in Fig. 6i show elevated values, reaching 37.57 wt% and 6.89 wt%, respectively. These findings

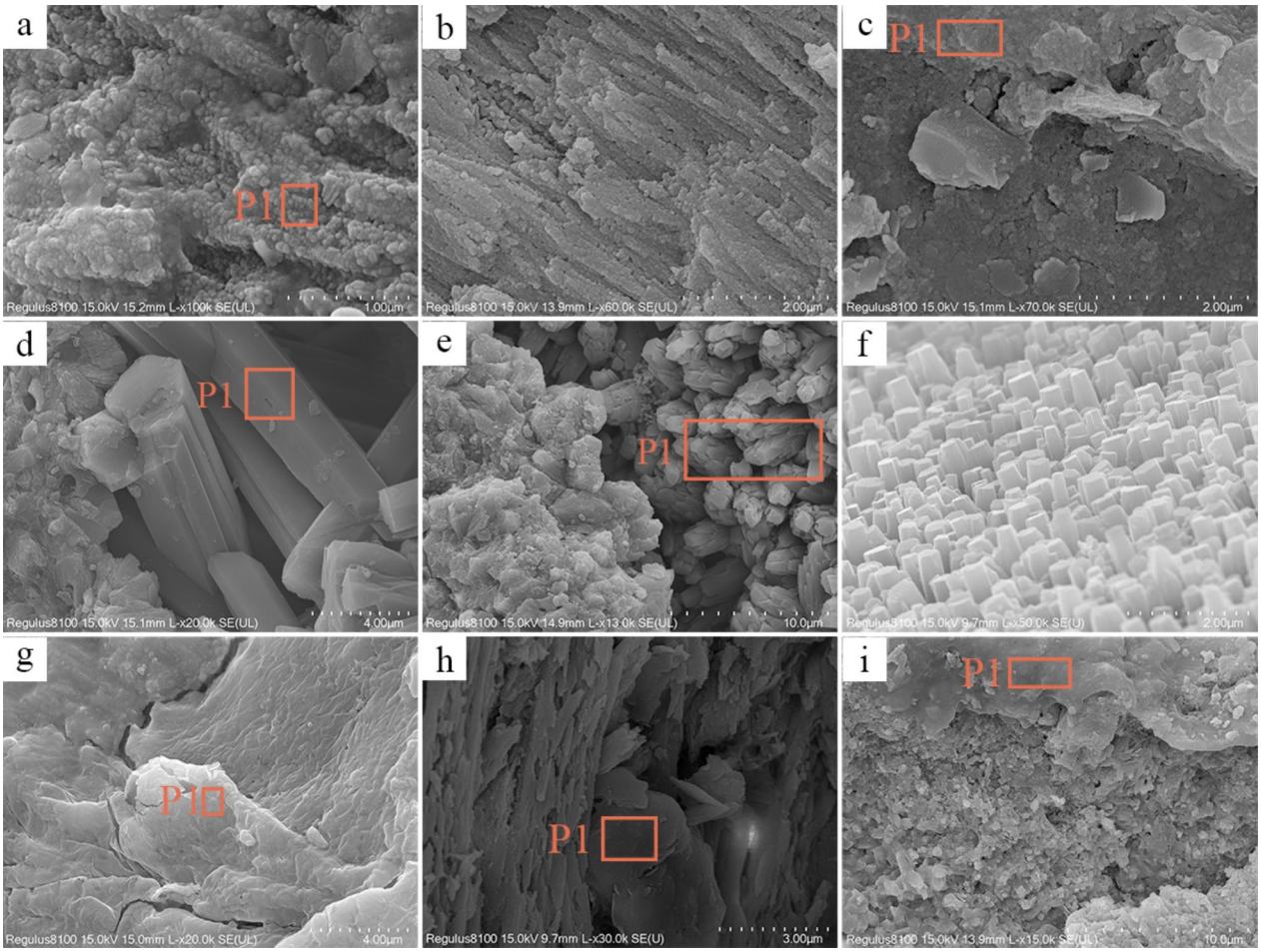

Fig. 6 Principle types of microstructures of tubular bio-concretions on the sherd sample. Position of **a**, **c**, **d**, **e** and **g** sequentially correspond to B1, B2, B3, B4, B5 noted in Fig. 4 **c**, while **f** and **h** correspond to B1 and B2 in Fig. 4d, respectively. **b** and **i** are scanning electron micrographs of sample N12. Red rectangles plotted in this figure indicate the regions of EDS analysis (EDS results see Table 2 below)

Table 2 Chemical composition of typical microstructures of tubular bio-concretion (wt%)

	Positions	C	N	O	Mg	Si	P	S	Ca	Mn	Fe
a	P1	14.65	1.38	45.09			1.22	0.87	36.39		
c	P1	10.08	2.51	14.83	2.20	5.54	5.00	2.80	35.19	11.34	3.17
d	P1	8.36	0.65	43.72			1.13	0.69	45.45		
e	P1	9.28	1.99	42.14			1.01	0.83	44.75		
g	P1	48.42	8.64	22.49		1.19	0.81	11.16	12.09		
h	P1	37.57		34.48	1.54	2.1	0.76	1.23	13.17		
i	P1	14.31	6.89	18.53		2.16	4.49	3.75	46.28	0.33	

strongly support the occurrence of organic substances in the analysed region.

The microstructures observed in panels h and i can be classified as oriented complex structures. The former may be associated with a lamella-fibrillar structure (LF), while the crystallites in the latter display an even higher degree of order, with axes aligned parallel to the tube wall. Furthermore, Fig. 5a reveals that the same growth increment comprises several zones with distinct yet highly ordered microstructures. Given the complex and oriented biomineral structures observed, an organic matrix-controlled crystallization model, proposed by

Vinn, might be much more suitable than a simple granular secretion model to explain the formation of these calcareous bio-tubes [24, 43]. SEM observations further reveal the interconnected and intergranular nature of the organic matrices, implying their precise control over the nucleation and growth of crystalline mineral phases [50, 51], as well as their ability to act as the adhesive binding together the biomineral particles [52]. Both the composition and quantity of organic components secreted by the benthic organisms play a crucial role in governing the formation process of shells and determining their overall mechanical properties [52]. It is widely accepted that the organic sheets enhances the mechanical properties of the tubes by serving as toughening agents during fracture. Through combining the strength of the biomineral layers with their own elasticity [48], they potentially preventing cracks from propagating within the structure [22].

Phase and structure analysis

As depicted in Fig. 7a, the XRD patterns obtained from samples N1, N6, N7 consistently exhibit six distinct diffraction peaks at 26.2°, 27.1°, 33.1°, 37.8°, 45.8° and 48.5°, corresponding to the (111), (021), (012), (112), (221), and (202) lattice plane of aragonite (PDF#71-2396), respectively. These observed diffraction peaks indicate the presence of aragonite as the predominant crystalline phase. The intensities of the peaks, however, exhibit notable variations among the samples, which can potentially be attributed to discrepancies in the concentration of organic matter or the presence of doped ions. Furthermore, additional diffraction peaks appearing at 29.9°, 40.0°, 43.7°, 49.3° can be well indexed to Ca(Mn,Ca)$(CO_3)_2$ (PDF#19-0234). This finding substantiates the results of obtained from the SEM–EDS analyses mentioned earlier, which confirmed the detection of elevated levels of manganese within a distinctive semicircular arc-shaped structure through EDS micro-area elemental analysis. The majority of the characteristic peaks observed in the XRD patterns of both aragonite and Ca(Mn,Ca)$(CO_3)_2$, as depicted in Fig. 7a exhibit sharp and intense, indicating a relatively high degree of crystallinity. However, each pattern also shows a broad peak centered at approximately 20.9°, suggestive of the presence of a certain quantity of amorphous matter. Although it is plausible that this amorphous matter may be attributed to nitrogen-containing organic compounds, further supporting evidence is necessary to ascertain this hypothesis. Moreover, it is noteworthy that no characteristic diffraction peaks corresponding to calcite are observed in the analysed samples. This absence may be attributed to its extremely low content and weak crystallization within the biomineral samples.

Thermogravimetric Analysis (TGA) along with Differential Thermogravimetry analysis (DTG) were performed to study the composition of this tubular bio-concretion and semi-quantitatively assess the level of its organic substrates, utilizing the same specimen (sample N6) as employed in the XRD analysis. DTG is recognized for its ability to unveil subtle shifts in weight-related phenomena. The TGA-DTG pattern in Fig. 7b reveals a major weight loss of 23.55% occurring within the temperature range from 672 to 745 °C (dark blue dash dotline in Fig. 7b). This range is in broad agreement with the previously reported decomposition temperature of $CaCO_3$, which typically occurs between 600 and 800 °C. During heating, the decomposition of calcium carbonate ($CaCO_3$) led to a weight loss. Notably the TG-DTG plot reveals a two-step decomposition process spanning from ~ 30 °C to 520 °C. The initial step, occurring < 200 °C, entails a minor alteration in sample mass (1.28%), primarily caused by the volatilization of low-molecule-weight acids and unbound water [22]. It is proposed that the subsequent stage of mass loss (1.65%) corresponds to the decomposition of the organic matrices. Collectively, these observations, in conjunction with the XRD patterns, suggests the tubular concretion is composed of $CaCO_3$ and organic matter.

Spectroscopic analysis of tubular biomineral composition

FT-IR analysis was conducted to further verify the composition of mineral phases and the presence of organic components. This analytical technique, along with Raman spectroscopy, provides complementary information to SEM–EDS and XRD analysis [53]. Figure 8a represents the characteristic peaks of both aragonite and calcite. Specifically, the absorption bands at 1450, 1082 and 715 cm^{-1} are indicative of aragonite, while the stretching vibrations at 1794 and 870 cm^{-1} should be assigned to calcite. Notably, the characteristic peak at 870 $cm^{-1} \pm$ might also be ascribed to biogenic aragonite [54]. Based on these observations, it is evident that the deposited calcareous tubes are predominantly biminerallic, in line with previous literature [26, 43]; however, considering the multiple characterization results mentioned earlier, aragonite appears to be the dominant polymorph. Additionally, the spectra reveal signals corresponding to the hydroxyl group present in hydro-carbonate within the range of 2520–2650 cm^{-1}.

In addition, a prominent peak centered at 2925 $cm^{-1} \pm$ is typically associated with either OH- or CH- stretching vibrations, indicating the potential presence of organic matter. Given the consensus regarding the occurrence of organic matrices in *serpulid* tubes [49] and the enduring plausibility of the hypothesis that biomacromolecule-controlled crystallization

underlies biomineralization [25], our attention is directed towards a specific spectral region ranging from 1700 to 1600 cm^{-1}. This region is recognized as the amide I band in IR spectra and can provide insights into the structural configurations of associated organic matrices [55, 59] since protein peptide bonds are amide groups (Table 3). By calculating the 2nd derivative of absorbance, several shoulder peaks become visible and their exact positions have been confirmed (Fig. 8b). The peaks at 1683, 1688 and 1694 cm^{-1} correspond to the amide I spectral signatures of the β-turn structure, a type of protein secondary structure, proving that certain types of protein might exist within the tubes. However, various amino acids are deemed to be the minor component of the soluble organic matrix. The primary constituents, which have the ability to bind cations and thereby influence the nucleation process, are identified as carboxylated and sulfated polysaccharides [25, 48].

Raman spectroscopy was conducted alongside the FT-IR analysis to collect phase and organic information about biominerals. This is necessary since the IR absorption peaks of organic-mineral composites often overlap, causing difficulties in data interpretation. Raman analysis, focusing on different positions of the bio-concretions, allows for the differentiation between calcite and aragonite. The peaks centered at 152, 207, 705, and 1087 cm^{-1} can be unambiguously attributable to aragonitic $CaCO_3$, whereas the peaks at 286 and 712 cm^{-1} ± indicate the presence of calcite. Notably, only spectrum 3 in Fig. 8c corresponds to the pure calcite phase, while spectrum 6 clearly reveals that the mineralogical composition of the investigated region is entirely aragonitic. In contrast, the other testing areas exhibit bimineralic characteristic. This finding is consistent with FT-IR and previous EDS analyses, demonstrating again that these tube-like calcareous concretions typically consist of both aragonite and calcite, with aragonite being more abundant. Aragonite rich calcareous structures are found to have a higher hardness and elasticity than that of calcite dominated crystal structures [60]. Additionally, a stretching band observed around 1520 cm^{-1} in the spectrum of sample N7 suggests a small amount of vaterite in the inorganic phase of this sample. This finding adds further complexity to the mineralogical composition of these bio-concretions.

Analogous to FT-IR, the protein secondary structures encompassing α-helices, β-sheets, β-turns and random structures, exhibit distinct signatures in a Raman spectrum, as indicated in Table 3 [56]. However, the

Table 3 Assignments of partial IR and Raman bands of protein secondary structures [55–58]

Secondary structures of proteins	Wavenumber of IR Amide I/cm^{-1}	Wavenumber of IR Amide III/cm^{-1}	Wavenumber of Raman Amide III/cm^{-1}
α-helix	1646–1661	1295–1330	1260–1340
β-turn	1615–1637	1220–1250	1270–1310
β-sheet	1665, 1670, 1675, 1683, 1688, 1694	1270–1295	1220–1265
Random coil	1637–1648	1250–1270	1230–1260

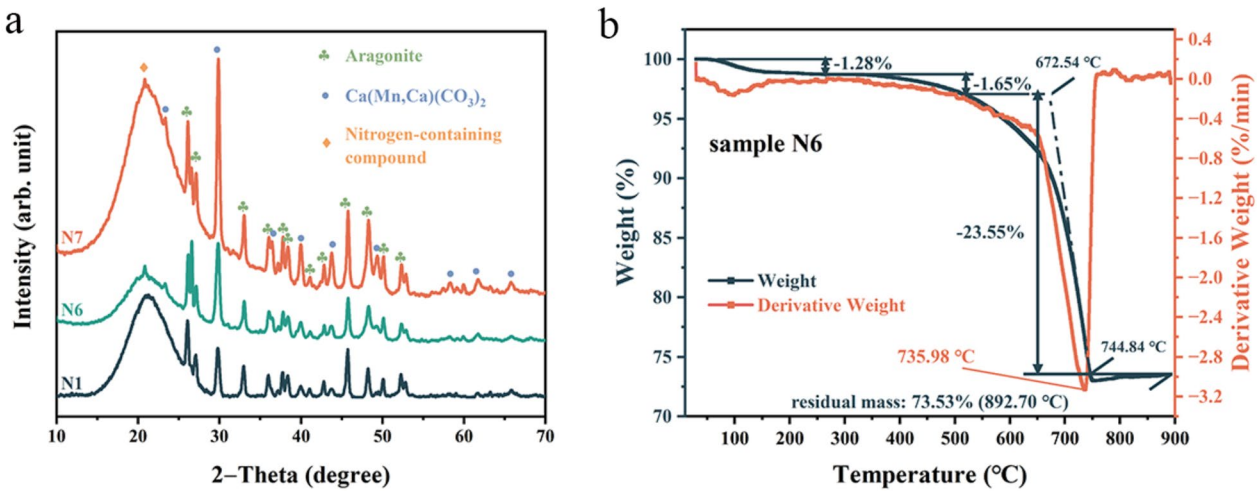

Fig. 7 XRD and Thermal analyses. **a** XRD patterns of sample N1, N6, and N7. **b** TGA-DTG pattern of sample N6

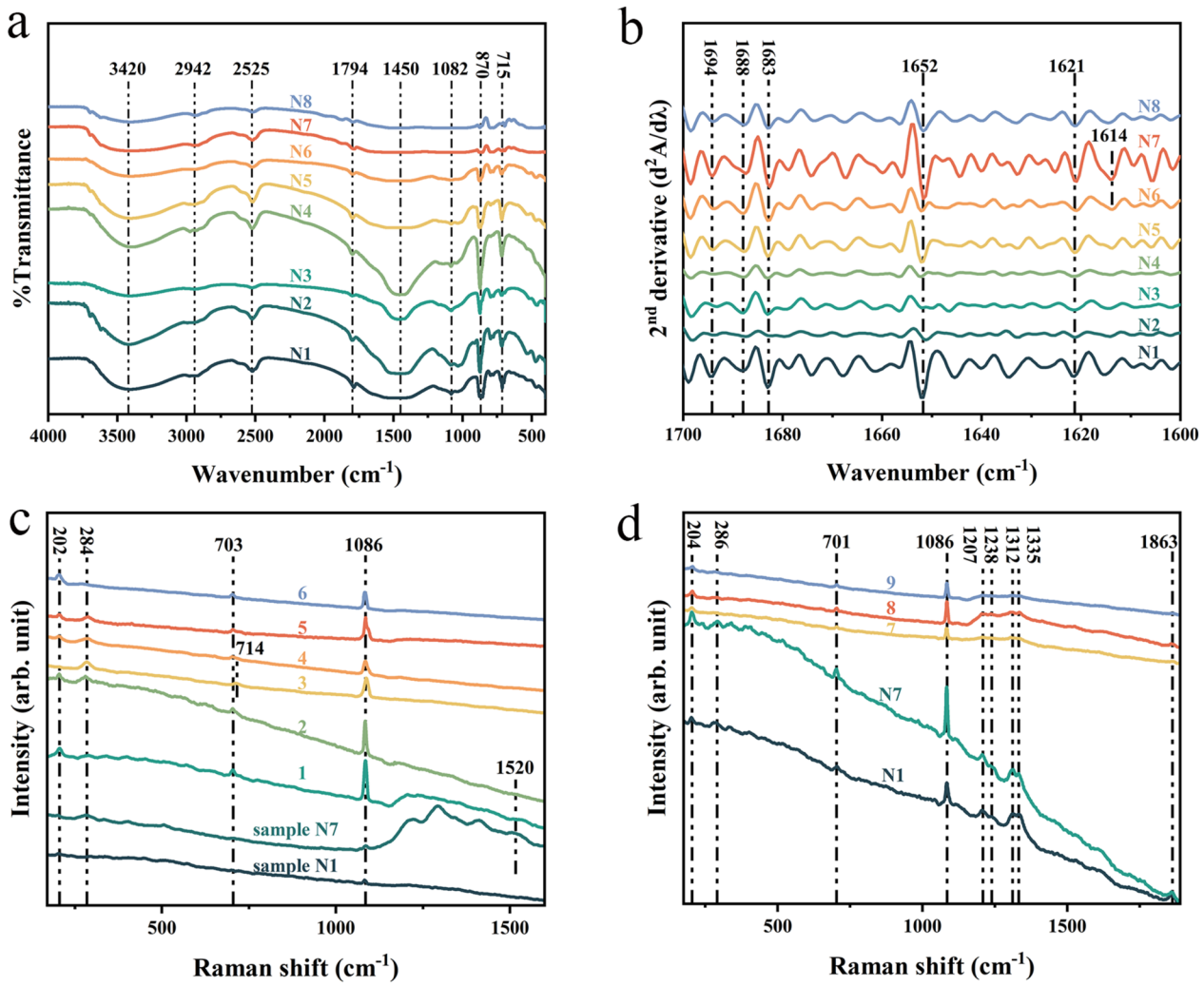

Fig. 8 FT-IR and Raman analysis of tubular type of bio-concretion samples. **a** FT-IR spectra of samples No.1–8. **b** Region of interest (amide I band) in the second order derivative spectra of each spectrum shown in **a**. **c** Raman spectra of sample N1, N7, and different positions on the fracture surfaces of sample N10 as well as N11 (the spot scanning points of spectra 1, 2, 3, 4 and 5 are marked in Fig. 4a, b with red dots). **d** Raman spectra of attachment surface of sample N1 and N7, along with Raman spectra of different positions at the interface between bio-concretions and glaze of sample N10 (the spot scanning points of spectra 7, 8 and 9 are marked in Fig. 4a with tiny red squares)

Raman bands corresponding to amide III, ranging from 1220–1400 cm^{-1}, are particularly useful as they are well-resolved and show minimal overlap compared to the amide I bands [57]. Figure 8d shows the Raman spectra obtained from the attachment surface of samples N1 and N7. In contrast to the spectra obtained from other positions of these same two samples (Fig. 8c), four new peaks are observed. Specifically, the peaks situated around 1312 and 1335 cm^{-1} can be assigned to the amide III, while the peaks at 1205 and 1860 cm^{-1} ± correspond to the C=S bond and the C=C bond, respectively, further corroborating the presence of organic substances. Considering previous research on biofouling [61], it is plausible to speculate that the observed peaks in the Raman spectra may be related to residual adhesive utilized by this tube-forming organism to adhere itself onto the underwater heritages. In addition, the spectra of regions 7, 8 and 9 show similarities to those of samples N1 and N7, presuming that the characteristic bands may originate from homologous organic substances. This suggests the existence of a protein-mediated bio-adhesion mechanism. Previous studies have also emphasized that the tubes of *H. elegans* adhere firmly to the submerged surfaces primarily through these adhesives, exhibiting greater resistance to dislodgement even compared to barnacles [61]. In the cement secreted by polychaeta tubeworms to

bond together the tubular shell materials, the modified amino acids present in the different adhesive proteins are assumed to also mediate physicochemical interactions with the substratum (i.e., adhesion) [62, 63].

Microscopic observations of biologically-induced degradation phenomena

The overall degradation morphologies of the glaze and the attachment forms of bio-concretions can be observed under OM and SEM with low magnification. As illustrated in Fig. 4, both sample N10 and N11 have been severely corroded, with extremely rough devitrification glaze surfaces. The interfaces between the tubular concretions and the glaze substrates were approximately illustrated by curves in Fig. 4a, b. Base on the information provided in Fig. 4, the depth range of the deposit layer is approximately 100–150 μm beneath the glaze surface. Their topography exhibited complex irregularities and undulations, indicative of a high-adhesion mechanical interlock structure [64].

Typical degradation morphology of glaze where bio-concretions attached

OM and SEM at low magnification were used to observe the cross-sectional degradation morphologies of the glaze layer for samples N11 (panels a, b, g and h) and N12 (panels e and k), as shown in the left-hand side of Fig. 9. It can be observed that the glaze surfaces exhibit a rough texture or even divided into several irregularly shaped areas mainly by cracks and craters (the former ~ 10 μm wide, the latter greater than 100 microns). The OM images (panels b and h) demonstrate that the glaze layer is almost opaque. The cross-sections of the samples show yellowish-white substances distributed in a banded pattern. Comparative analysis of panels g and h reveals that these yellowish-white regions typically consist of multiple interconnected craters, containing numerous randomly interlaced lamellar or plate-like crystals. And there are interstices between crystals and the glass phase created by corrosion. The prevailing view holds that when the corrosion channels in the glaze are interconnected, it can readily facilitate the complete delamination or spalling of the upper glaze layer [65]. Therefore, it can be inferred that the interconnected network of craters formed during the degradation processes is the primary cause of glaze surface concavities observed in panels e and k. In addition, the presence of black-brown regions proximal to the glaze surface corresponds to the remnant glass phase, as evidenced in panels a and b. The above-mentioned phenomena reflect the severe degradation that the glass phase has generally undergone in the case of such tubular bio-concretions attached to the celadon surfaces. Numerous pits, cracks and pores can be observed in the micrograph shown in Fig. 9. These features are possibly the result of multiple corrosive factors, such as mechanical forces applied by sand and debris particles, as well as the biological activities of macrobenthic organisms.

On the right-hand side of Fig. 9 are the further magnified SEM images demonstrating the finer details of the glaze degradation microstructure. The elemental composition results of typical degradation phases obtained from EDS analysis are shown in Table 4. Panels c and d collectively illustrate a kind of submicron porous microstructure surrounded by densely spaced, short column-like crystals. Based on the EDS analysis, these columnar crystals are very likely to be the anorthite ($CaAl_2Si_2O_8$). Existing research has shown that anorthite crystals in ancient Chinese calcium glazes are frequently accompanied by phase-separated structures susceptible to corrosion [66, 67]. The selective dissolution of the CaO-rich droplet phase within this structure typically occurs after prolonged seawater exposure, causing part of the residual glaze in the craters to exhibit a porous microstructure, akin to what is observed in our research samples. This process may lead to the depletion of Ca and the relative enrichment of Si. However, the EDS analysis at position 1 in panel c reveals remarkably high Ca and relatively low Si content, contradicting the above degradation patterns [68]. In contrast, the EDS result of the analogous degradation micromorphology shown in panel f is consistent with previous research findings. It is also suggested that these small holes may gradually connect after further corrosion, forming porous channels and cracks [9]. This would enable much more seawater to enter the glaze, eventually accelerating the disintegration of the SiO_2-rich continuous phase. Panel f also exhibits randomly packed layers of spherical colloidal particles near the glass phase region. These spherical aggregates are with a size of ~ tens of nanometers and rich in SiO_2 (see Table 4). Multiple studies have adopted the mechanism of interface-coupled dissolution–precipitation (ICDP) to explain the occurrence of this corrosion phenomenon [65, 68]. Panels i, j and l are the magnified SEM images of the yellowish-white corrosion region on the cross-sections of samples N11 and N12. There are some interwoven lamellar phases permeating and precipitating within the interstices of anorthite microcrystals. The SiO_2 content of this lamellar structure is much lower than the glaze, while the MgO and Al_2O_3 contents are relatively high, at 16.07% and 12.25%, respectively (Table 4). Mg^{2+} in seawater enters the glaze layer through the previously mentioned channels formed by the alternative dissolution of the phase separation. These ions react with Al^{3+} and other cations released from the glaze, leading to the precipitation of this corrosion product.

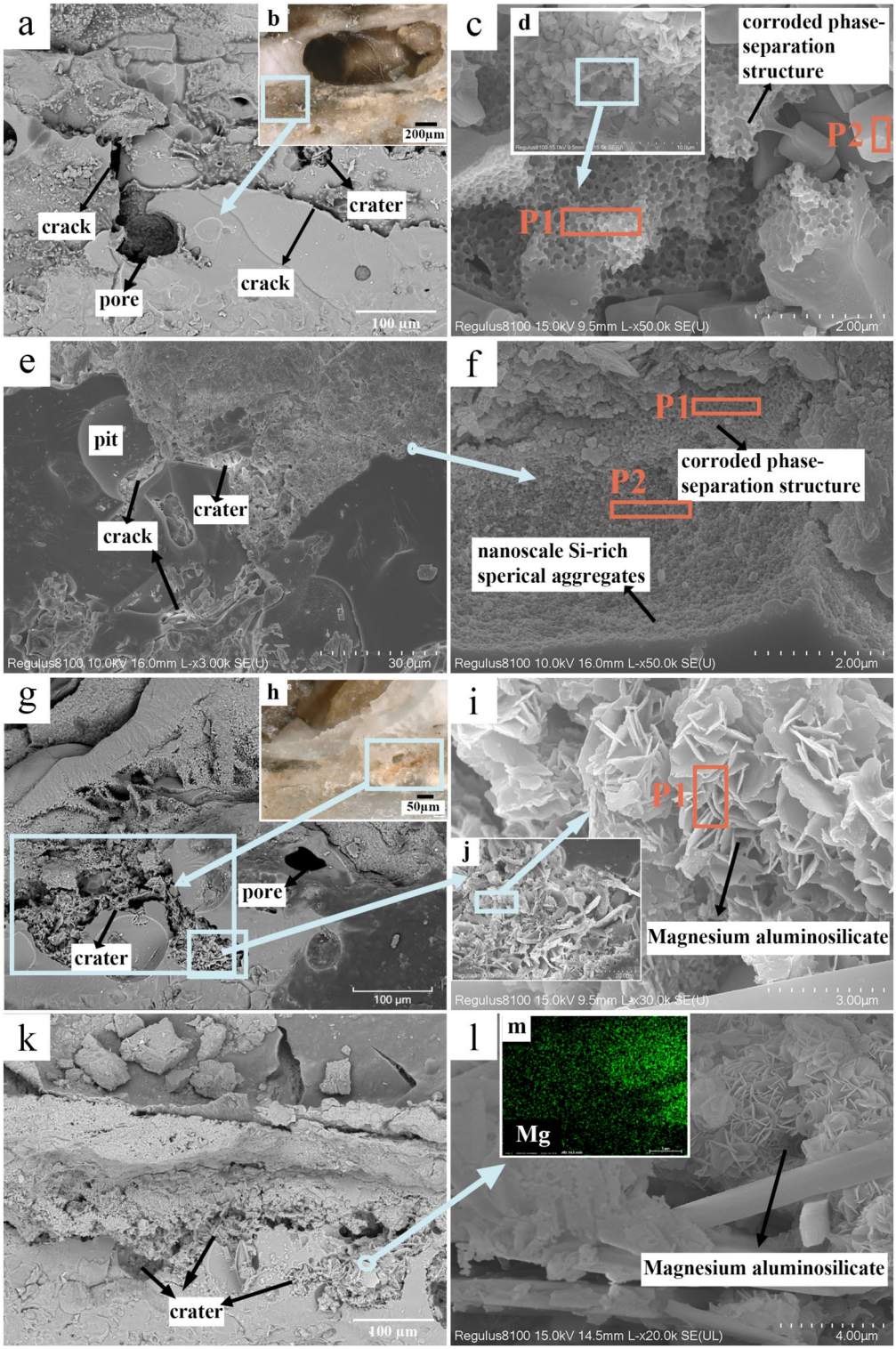

Fig. 9 Typical degradation morphologies of glaze of sample N11 and N12. **a** and **g** low magnification SEM images of sample N11. **b** and **h** optical microscopy images of different regions of sample N11, with blue rectangles indicating the sample areas corresponding to the SEM images **a** and **g**. **e** and **k** low magnification SEM images of sample N12. **c**, **d**, **i**, and **j** high magnification SEM images of sample N11, of which **i** and **j** are the enlarged view of corrosion crater illustrated in **g**. **f** and **l** the enlarged view of corrosion craters in **e** and **k**, respectively. **m** the EDS mapping result of **l**. Red rectangles plotted in this figure indicate the regions of EDS analysis (EDS results see Table 4 below)

Table 4 Chemical compositions of the marked positions in glaze typical degradation regions (in atomic%)

	Positions	C	O	Mg	Al	Si	P	S	Ca	Fe	Possible phase
c	P1	26.96	20.22		14.73	6.49	0.42	0.42	23.03	1.15	Corroded phase-separation structure
c	P2	25.67	32.64		10.76	8.71	0.58	0.73	20.51		Anorthite
f	P1	24.56	41.75	0.52	3.31	17.96	3.45	2.24	3.73	0.33	Corroded phase separation structure
f	P2	37.28			3.33	35.03	6.86	4.32	8.01	0.80	Silica spherules/Silica-rich gel
i	P1	31.19	42.58	9.69	6.31	2.91	1.63	1.09	0.98	1.14	Magnesium aluminosilicate

Interface morphologies between the bio-concretions and the glaze

High-magnification SEM observations of sample N10 reveal two distinct bio-concretion-glaze interface forms. The first type involves the direct deposition of bio-concretions on the silica-rich gel, which is a secondary phase formed via the ICDP mechanism (Fig. 10a, b). The second type showcases bio-concretions accumulating in corrosion craters—created by the alternative dissolution of the two separated glass phases and the subsequent shedding of anorthite crystals (Fig. 10c, d). The SEM images show that oriented or semi-oriented nanoparticles are commonly found densely distributed at the interface and exhibit a layered arrangement in the two-dimensional plane. This indicates that the precipitation and biomineralization of $CaCO_3$ have undergone a template influence by organic matter. Alongside these structures, lamellar structures and unoriented nanoparticles are also observed in contact with the glaze layer. Furthermore, as can be seen in Fig. 10b, cracks traversing the glaze layer are potentially induced by the compressive stress and other mechanical damage forms from the bio-concretions.

As illustrated in insets ii & iii of Fig. 10a and c, the EDS mapping results indicates spatial correlation between elements: the higher the content of Si, and the lower the content of Ca. At the bio-concretions side, the closer to the interface, the higher the content of Si. Previous experiments have indicated a scarcity of Si elements in the bio-concretions, suggesting that they originate primarily from the glaze layer. As these bio-concretions are deposited on the Si-rich gel, their formation may be associated with the hydrolysis of the glaze. Moreover, both point analysis and area mapping demonstrate the

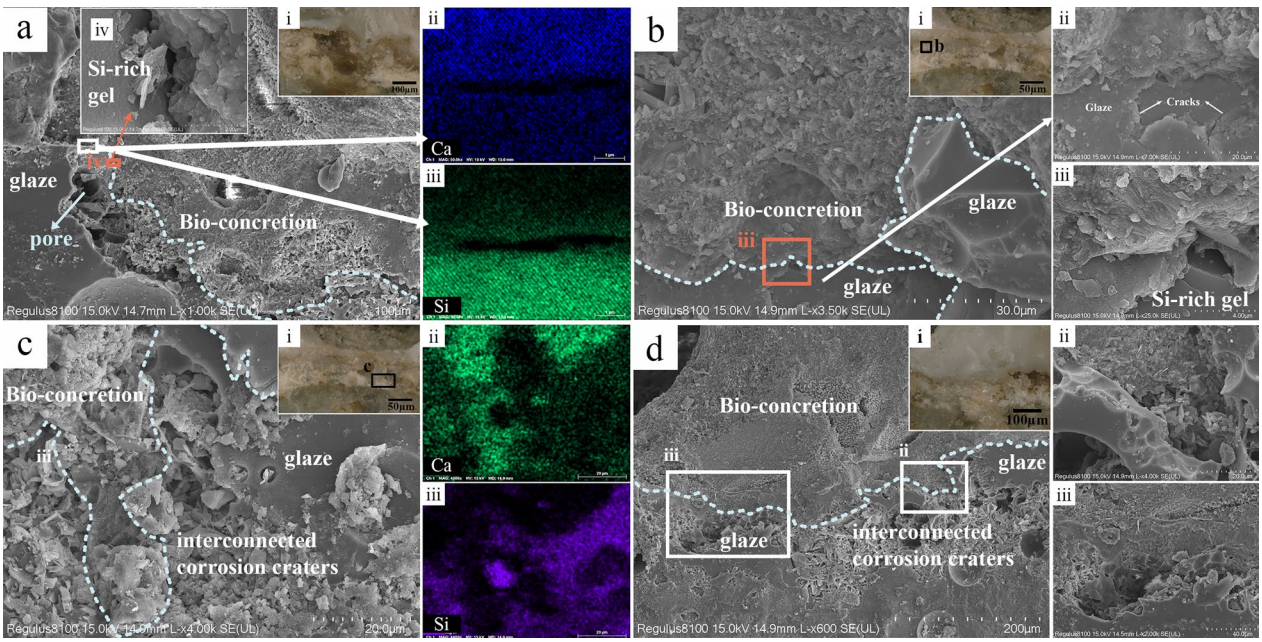

Fig. 10 Typical bio-concretions-glaze interface morphologies of sample N10. **a**, **b**, **c**, and **d** different regions of interface of sample N10. **i** of each panel are the OM images of sample N10 showing the specific regions imaged by SEM. **ii** and **iii** of panel **a** the EDS mapping results of regions in a plotted by white rectangle. **ii** and **iii** of panel **c** the EDS mapping results of **c.** Red rectangles highlight the areas where the silica-rich gel layers can be clearly observed

enrichment of the element P near the interface, with its content remaining almost consistent at both ends. Given the close association of P with organic matter in organisms, it could serve as a biomarker for the existence of life activity in geological bodies. The migration of P may indeed occur, or the glaze surfaces may undergo a progression from the initial coating of adsorbed organic molecules to the formation of biofilms.

Discussion of biofouling-driven degradation

The interconnected craters, the submicron porous microstructures of the residual glaze, the aggregated silica-rich spherules/silica-rich gel, and the MgO-rich interwoven lamellar corrosion products are the primary corrosion phenomena of the glaze to which tubular bio-concretions attached. This is basically consistent with the corrosion morphologies of glaze layers in the marine environments that have not been subjected to biofouling by large benthic organisms. However, the complete devitrification of the glaze layer, substantial loss of the glass phase, the thorough alteration of the celadon's surface color, increased roughness, and more pronounced unevenness of the glaze surface, all indicate that the degree of corrosion is significantly higher than that of the latter. This suggests that the glaze layer have also suffered severe damage from biofouling, in addition to physical damage and chemical corrosion. The combined effects of them may lead to more severe degradation.

For the glaze where tubular bio-concretions attached to, we propose a possible corrosion pathway in the form of schematic illustration, as shown in Fig. 11, based on the microscopic analyses and existing research concerning biofouling. Once the celadon was submerged, conditioning film and biofilm successively formed. When the larvae of polychaeta tubeworms are attracted by biofilm signals, mainly from Pseudoalteromonas [69], they massively aggregate and grow on the exterior of algal spores and protozoans [61]. Subsequently, the tubeworms construct their protective tubes by secreting calcium carbonate slurry. It is inferred that they may directly utilize Ca^{2+} as well as Si and other elements—generated by the hydrolysis of the silicate framework and the selective dissolution of CaO-rich droplets phase—as the slurry raw materials. Under the influence of their own secreted organic matter, they precipitate mechanically robust bio-concretions through biomineralization process within the corrosion craters on the glaze surface. Multi-factor coupling effects, such as microbially-induced calcite precipitation (MICP) [70] pathways, biological metabolites, mechanical abrasion from biological activities of large benthic organisms, and other common forms of mechanical damage as well as chemical corrosion, lead to the breakage of the glass structure, and the formation as well as extension of cracks. These defects provide rapid channels for external corrosive agents to enter the glaze, facilitating the loss of the glass phase and the shedding of crystals, and eventually leading to the formation of corrosion craters. Furthermore, these robust bio-concretions deposited inside the glaze layer may potentially exacerbate the propagation of cracks and the enlargement of

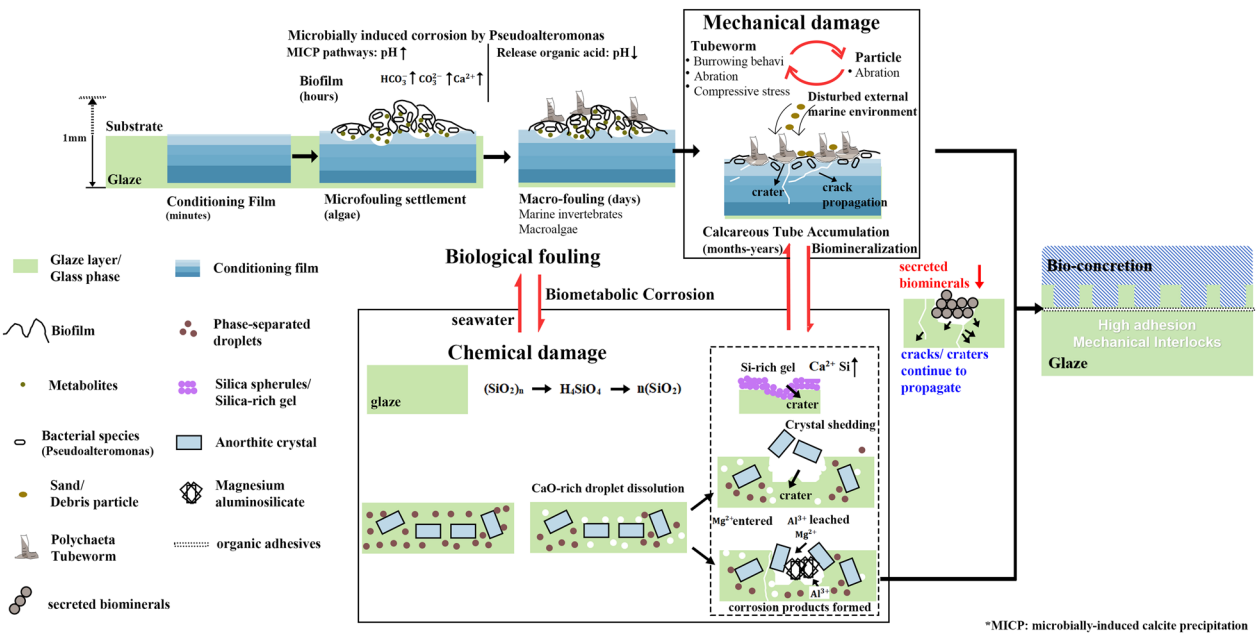

Fig. 11 Schematic illustration of the possible degradation process of the glaze where tubular bio-concretions attached

corrosion craters. These bio-concretions are characterized by highly adhesive mechanical interlocks with the glaze layer, resulting in a firm attachment that is resistant to dislodgement.

Conclusion

This study presents a thorough investigation of the tubular bio-concretions on Longquan celadon from the Shengbeiyu shipwreck, employing a multi-analytical approach. The findings reveal that these bio-concretions are predominantly composed of aragonite with lesser amounts of calcite, and they exhibit complex yet highly ordered microstructures. The presence of organic matter within the bio-concretions suggests an organic matrix-controlled crystallization process, a common feature in benthic calcareous tubes. Microscopic and spectroscopic analyses indicate that the bio-concretions intricately intermesh with the celadon's glaze, which displays significant corrosion patterns and contributes to significantly enhanced interfacial adhesion. The detection of proteins at the bio-concretion and glaze interface points to bio-adhesion mechanisms mediated by organic substances. These insights enhance our understanding of the biomineralization processes and the biofouling dynamics affecting submerged ceramics, providing valuable information for developing effective conservation strategies for underwater cultural heritage of various other materials.

Abbreviations

NCA	National Centre for Archaeology
XRD	X-ray diffraction
OM	Optical microscopy
SEM–EDS	Scanning electron microscopy with energy-dispersive X-ray spectroscopy
Micro-CT	Micro-Computed tomography
FT-IR	Fourier transform infrared spectroscopy
TGA	Thermogravimetric analysis
DTG	Differential thermogravimetry analysis
RT	Room temperature
SCC	Stress corrosion cracking
ICDP	Interface-coupled dissolution–precipitation
MICP	Microbially-induced calcite precipitation

Acknowledgements

The authors extend their sincere appreciation to Guoqing Liang from the National Centre for Archaeology (the NCA) for providing the Longquan celadon sample, significantly enhancing the research's scope and depth. The base-map, indicating the geographical location of the Shengbeiyu shipwreck site, was provided by the Level-1 and Atmosphere Archive & Distribution System (LAADS) Distributed Active Archive Center (DAAC) at the Goddard Space Flight Center in Greenbelt, Maryland. The authors acknowledge LAADS DAAC for their efforts in processing, archiving, and distributing remote sensing-derived Earth science data products.

Author contributions

X.H. and J.Z. made substantial contributions to the conception and design of the work. X.L. undertook experimental work, wrote the manuscript text, analysed the data and prepared all the Figures; X.L, Y.L. and J.Z did the formal analysis and investigation. X.H and Y.L provided advice on the study design and revised the work critically; H.W provided samples and funding. All authors have read and agreed to the published version of the manuscript.

Funding

This research was funded by the National Key R&D Program of China, grant number 2023YFF0906403.

Availability of data and materials

The datasets used and/or analysed during the current study are available from the corresponding author on reasonable request.

Declarations

Competing interests

The authors declare that they have no competing interests.

Author details

[1]Key Laboratory of Archaeomaterials and Conservation, Ministry of Education, Institute for Cultural Heritage and History of Science and Technology, University of Science and Technology Beijing, Beijing 100083, China. [2]Institute of High Energy Physics, Chinese Academy of Sciences, Beijing 100049, China. [3]National Centre for Archaeology, Beijing 100013, China.

Received: 4 April 2024 Accepted: 27 June 2024
Published online: 11 July 2024

References

1. Yang Z, Deng Q, Liu M. Ancient Shipwrecks off the Coast of Zhangzhou, Fujian. In: Song J, editor. Shipwreck archaeology in China Sea. The archaeology of Asia-Pacific navigation. Singapore: Springer; 2022. p. 135–61.
2. National Centre of Archaeology, Fujian provincial research institute of archaeology, Zhangzhou Cultural Relics Protection Center. A Report on the Archaeological Survey and Research into the Shipwrecks on Shengbeiyu Island, Zhangzhou. Palace Mus J. 2023; 48–59+126–127.
3. Yang Z. Archaeological survey of Yuan Dynasty shipwrecks near Shengbeiyu Island, Zhangzhou. Cult Relics East. 2015; 69–78.
4. Florian M-LE. The underwater environment. Conserv Mar Archaeol Objects. Amsterdam, Netherlands: Elsevier; 1987.
5. Crisci GM, La Russa MF, Macchione M, Malagodi M, Palermo AM, Ruffolo SA. Study of archaeological underwater finds: deterioration and conservation. Appl Phys A. 2010;100:855–63.
6. López-Arce P, Zornoza-Indart A, Gomez-Villalba L, Pérez-Monserrat EM, Alvarez De Buergo M, Vivar G, et al. Archaeological ceramic amphorae from underwater marine environments: influence of firing temperature on salt crystallization decay. J Eur Ceram Soc. 2013;33:2031–42.
7. Casoli E, Ricci S, Belluscio A, Gravina MF, Ardizzone G. Settlement and colonization of epi-endobenthic communities on calcareous substrata in an underwater archaeological site. Mar Ecol. 2014;36:980–992.
8. Ricca M, Cámara B, Fort R, Álvarez de Buergo M, Randazzo L, Davidde Petriaggi B, et al. Definition of analytical cleaning procedures for archaeological pottery from underwater environments: the case study of samples from Baia (Naples, South Italy). Mater Des. 2021;197:109278.
9. He Y, Li W, Li J, Xu C, Lu X. Corrosion of Longquan celadons in the marine environment: study on the celadons from the Dalian Island shipwreck of the Yuan Dynasty. Herit Sci. 2021;9:104.
10. He Y, Li W, Xu C, Lu X, Sun X. Degradation mechanism of the Ru wares unearthed from the Qingliangsi site in Henan, China. Ceram Int. 2022;48:17131–42.
11. Aloise P, Ricca M, La Russa MF, et al. Diagnostic analysis of stone materials from underwater excavations: the case study of the Roman archaeological site of Baia (Naples, Italy). Appl Phys A. 2013;114:655–62.
12. Xiaoyan He. Formation and regulation mechanisms of conditioning layer and biofilm during marine biofouling. University of Chinese Academiy of Sciences (Ningbo Institute of Materials Technology & Engineering Chinese Academy of Sciences); 2018.

13. Hao X, Zhu T-Q, Xu J-J, Wang Y-R, Zhang X-W. Microscopic study on the concretion of ceramics in the " Nanhai I " shipwreck of China, Southern Song Dynasty (1,127–1,279 A.D.). Microsc Res Tech. 2018;81:486.
14. Bao C, Jia S, Yan Fu, Liu A. Analysis of the concretion on the surface of the greenish white porcelain artefacts from Huaguang Reef I. Chem Res. 2014;25:76–81.
15. Ye D. Study on the coagulation in the Shipwreck archaeology. Museum. 2019;4:24–30.
16. Wang Y, Zhu T, Yang G, Tan X, Ye D, Chen H. The method to soften the concretions of ceramics in the "Nanhai I" Shipwreck of China Southern Song Dynasty (1127–1279AD). Herit Sci. 2018;6:4.
17. Liu X. Study on the types of the concretion covered on the surface of the ceramics in "Nan'ao I" shipwreck. Fujian Wenbo. 2021; 51–8.
18. Du J. The comprehensive evaluation for desalination and concretion cleaning of marine ceramics_ according to the example of "Nan'ao I" and "Nanhai I". [Beijing]: University of Chinese Academiy of Sciences; 2016.
19. Dongbo Hu, Zhang H. A study on the impacts of commonly-used porcelain cleaning agents. Sci Conserv Archaeol. 2010;22:49–59.
20. Li W, Chen Y, Li N, Li B, Luo W. A study on quantitative evaluation of damage in conservation of ceramics from Huaguangjiao I Shipwreck with ICP-AES. Spectrosc Spectr Anal. 2015;35:772–6.
21. Zhao M, Zhai Y, Zhao J, Zhou W, Zhao L, Ge Y, et al. Microbial corrosion on underwater pottery relics with typical biological condensation disease. Herit Sci. 2023;11:260.
22. Hou X. Study on fine structure and mechanical properties of sea shells. Hainan University; 2021.
23. Xie L. Microstructure and formation mechanism of nacre of H. Cumingii lea shell and the growth of nacreous coatings. Zhejiang University; 2011.
24. Vinn O, Kirsimäe K, ten Hove H. Tube ultrastructure of Pomatoceros americanus (Polychaeta, Serpulidae): implications for the tube formation of serpulids. Est J Earth Sci. 2009. https://doi.org/10.3176/earth.2009.2.05.
25. Vinn O. Biomineralization in polychaete annelids: a review. Minerals. 2021;11:1151.
26. Chan VBS, Vinn O, Li C, Lu X, Kudryavtsev AB, Schopf JW, et al. Evidence of compositional and ultrastructural shifts during the development of calcareous tubes in the biofouling tubeworm. Hydroides elegans J Struct Biol. 2015;189:230–7.
27. Chen S, Wang W, Li Q. Assessment of environmental quality in seawater and sediment of Futou Bay, Fujian. Environ Sustain Dev. 2017;42:156–8.
28. The navigation guarantee department of the Chinese navy headquarters. China sailing directions East China Sea. China Navigation Book Publishing House; 2010.
29. Level-1 and Atmospheric Data. https://ladsweb.modaps.eosdis.nasa.gov/view-data/#@0.0,0.0,3.0z. Accessed 20 Mar 2024.
30. Cairns SD, Kitahara MV. An illustrated key to the genera and subgenera of the recent azooxanthellate Scleractinia (Cnidaria, Anthozoa), with an attached glossary. ZooKeys. 2012;227:1–47.
31. Cunningham JA, Rahman IA, Lautenschlager S, Rayfield EJ, Donoghue PCJ. A virtual world of paleontology. Trends Ecol Evol. 2014;29:347–57.
32. Carvalho LE, Sobieranski AC, von Wangenheim A. 3D segmentation algorithms for computerized tomographic imaging: a systematic literature review. J Digit Imaging. 2018;31:799–850.
33. Hu Y Z, Limaye A, Lu J. A 3D segmentation & reconstruction method in paleontology using Drishti. Bio-Protoc. 2021;101:e1010668. https://doi.org/10.21769/BioProtoc.1010668
34. de Messano LVR, Sathler L, Reznik LY, Coutinho R. The effect of biofouling on localized corrosion of the stainless steels N08904 and UNS S32760. Int Biodeterior Biodegrad. 2009;63:607–14.
35. Antoniadou C, Voultsiadou E, Chintiroglou C. Benthic colonization and succession on temperate sublittoral rocky cliffs. J Exp Mar Biol Ecol. 2010;382:145–53.
36. Lin J, Wang J, Lin H, He X, Huang Y, Li R, et al. Studies on the macrobenthic diversity in the water around Gulei Peninsula of Fujian in spring. Prog Fish Sci. 2015;36:23–9.
37. Yan T, Zhang H, Li Y, Cao W, Biru Hu. An overview of fouling sedentary polychaetes. Acta Ecol Sin. 2014;34:6049–57.
38. Jin-xiang J. Ecological research of marine fouling in Dongshan Bay, China. Acta Oceanol Sin. 2012;34:160–169.
39. Yu H-P, Zhu Y-J. Guidelines derived from biomineralized tissues for design and construction of high-performance biomimetic materials: from weak to strong. Chem Soc Rev. 2024. https://doi.org/10.1039/D2CS00513A.
40. Vinn O, Kupriyanova EK. Evolution of a dense outer protective tube layer in serpulids (Polychaeta, Annelida). Carnets de Géologie. 2011;5:137–47.
41. Vinn O, Mutvei H, Ten Hove HA, Kirsimä EK. Unique Mg-calcite skeletal ultrastructure in the tube of the serpulid polychaete Ditrupa. Neues Jahrb Für Geol Paläontol - Abh. 2008;248:79–89.
42. Berent K, Gajewska M, Checa AG. Organization and formation of the crossed-foliated biomineral microstructure of limpet shells. ACS Biomater Sci Eng. 2023;9:6658–69.
43. Vinn O, ten Hove H, Mutvei H, Kirsimäe K. Ultrastructure and mineral composition of serpulid tubes (Polychaeta, Annelida). Zool J Linn Soc. 2008;154:633–50.
44. Vinn O. On the unique isotropic aragonitic tube microstructure of some serpulids (Polychaeta, Annelida). J Morphol. 2013;274:478–482.
45. Buckman JO. An overview of the tube fabric of Pomatoceros (Polychaeta, Serpulidae), illustrated by examples from the British Isles. Zool Anz - J Comp Zool. 2015;259:54–60.
46. National Center for Archaeology, Fujian Provincial Archaeological Research Institute, Zhangzhou Cultural Relics Protection Center. Archaeological Report on the Yuan Dynasty Shipwreck on Shengbeiyu Island in Zhangpu: KeySurveys in 2021. Cultural Relics Press.
47. Chan VBS, Li C, Lane AC, Wang Y, Lu X, Shih K, et al. CO2-driven ocean acidification alters and weakens integrity of the calcareous tubes produced by the Serpulid Tubeworm, Hydroides elegans. PLoS ONE. 2012;7:e42718.
48. Vinn O. Occurrence, formation and function of organic sheets in the mineral tube structures of Serpulidae (Polychaeta, Annelida). PLoS ONE. 2013;8:e75330.
49. Tanur AE, Gunari N, Sullan RMA, Kavanagh CJ, Walker GC. Insights into the composition, morphology, and formation of the calcareous shell of the serpulid Hydroides dianthus. J Struct Biol. 2010;169:145–60.
50. Li X, Li S, Huang X, Chen Y, Cheng J, Zhan A. Protein-mediated bioadhesion in marine organisms: a review. Mar Environ Res. 2021;170:105409.
51. Becker PT, Lambert A, Lejeune A, Lanterbecq D, Flammang P. Identification, characterization, and expression levels of putative adhesive proteins from the tube-dwelling polychaete Sabellaria alveolata. Biol Bull. 2012;223:217–25.
52. Huang W, Restrepo D, Jung J, Su FY, Liu Z, Ritchie RO, et al. Multiscale toughening mechanisms in biological materials and bioinspired designs. Adv Mater. 2019;31:1901561.
53. Tao J. FTIR and Raman studies of structure and bonding in mineral and organic-mineral composites. In: De Yoreo JJ, editor. Methods enzymol. San Diego, CA: Academic Press; 2013.
54. Zhang G, Li H. The FTIR spectra difference between biogenic and abiogenic aragonites. Miner Petrol. 2006;26:1–4.
55. Ye S, Li H, Yang W, Luo Y. Accurate determination of interfacial protein secondary structure by combining interfacial-sensitive amide I and amide III spectral signals. J Am Chem Soc. 2014;136:1206–9.
56. Kuhar N, Sil S, Umapathy S. Potential of Raman spectroscopic techniques to study proteins. Spectrochim Acta A Mol Biomol Spectrosc. 2021;258:119712.
57. Oladepo SA, Xiong K, Hong Z, Asher SA, Handen J, Lednev IK. UV resonance Raman investigations of peptide and protein structure and dynamics. Chem Rev. 2012;112:2604–28.
58. Vedantham G, Sparks HG, Sane SU, Tzannis S, Przybycien TM. A holistic approach for protein secondary structure estimation from infrared spectra in H2O solutions. Anal Biochem. 2000;285:33–49.
59. Ji Y, Yang X, Ji Z, Zhu L, Ma N, Chen D, et al. DFT-calculated IR spectrum amide I, II, and III band contributions of N-Methylacetamide fine components. ACS Omega. 2020;5:8572–8.
60. Pérez-Huerta A, Cusack M, Zhu W. Assessment of crystallographic influence on material properties of calcite brachiopods. Mineral Mag. 2008;72:563–8.
61. Nedved BT, Hadfield MG. Hydroides elegans (Annelida: Polychaeta): a model for biofouling research. In: Flemming H-C, Murthy PS, Venkatesan R, Cooksey K, editors. Mar Ind Biofouling. Berlin: Springer; 2009. p. 203–17.
62. Stewart RJ, Wang CS, Shao H. Complex coacervates as a foundation for synthetic underwater adhesives. Adv Colloid Interface Sci. 2011;167:85–93.
63. Zhao H, Sun C, Stewart RJ, Waite JH. Cement Proteins of the Tube-building Polychaete Phragmatopoma californica. J Biol Chem. 2005;52:42938–44.

64. Zhu M, Zhang F, Chen X. Bioinspired mechanically interlocking structures. Small Struct. 2020;1:2000045.
65. Zhou B, Ma Q, Li Z, Zhang Z, Li N. Corrosion of glaze in the marine environment: study on the green-glazed pottery from the Southern Song "Nanhai I" shipwreck (1127–1279 A.D.). Herit Sci. 2023. https://doi.org/10.1186/s40494-023-00965-w.
66. Li W, Li J, Deng Z, Wu J, Guo J. Study on Ru ware glaze of the Northern Song dynasty: one of the earliest crystalline-phase separated glazes in ancient China. Ceram Int. 2005;31:487–94.
67. Li W. Glazes in China. Dordrecht: Springer; 2014. p. 1–11.
68. He Y, Li W, Li J, Xu C, Lu X. Research on the degradation of ancient Longquan celadons in the Dalian Island shipwreck. Npj Mater Degrad. 2022;4:1–10.
69. Lau SCK, Qian P-Y. Larval settlement in the serpulid polychaete Hydroides elegans in response to bacterial films: an investigation of the nature of putative larval settlement cue. Mar Biol. 2001;138:321–8.
70. Vuong P, McKinley A, Kaur P. Understanding biofouling and contaminant accretion on submerged marine structures. Npj Mater Degrad. 2023;7:1–11.

Publisher's Note